



Investigation of material removal mechanisms of laser-structured Si_3N_4 via single diamond grit scratching

Masih Paknejad¹ · Bahman Azarhoushang¹ · Ali Zahedi¹ · Mehdi Khakrangin¹ · Mohammad Ali Kadivar¹

Received: 22 August 2022 / Accepted: 27 December 2022 / Published online: 26 January 2023
© The Author(s) 2023

Abstract

Grinding hard-brittle materials like silicon nitride is faced with some challenges, including sub-surface damage, high tool wear, and low grinding efficiency. Ultrashort-pulse laser structuring of hard materials prior to the grinding process significantly reduces the cutting forces and temperature and increases the achievable material removal rate of the grinding process. These effects are partially due to controllable induced damages into the subsurface of the structured workpieces. However, the impacts of this surface structuring technique on the material removal mechanism of advanced ceramics, such as Si_3N_4 , are not yet thoroughly investigated. The dominant material removal mechanism in grinding hard and brittle materials, such as silicon nitride (Si_3N_4), defines the surface integrity of the workpiece. For the first time, in-depth single diamond grit scratching experiments are carried out to investigate the changes in the dominant material removal mechanisms at various chip thicknesses by laser structuring of Si_3N_4 . Two different structuring ratios (25% and 50%) were generated on sample surfaces by a femtosecond laser. The effects of laser structuring on material removal mechanism, pile-up area, area and width of the groove, grit path, normal and tangential forces, and specific cutting energy have been investigated. The results indicate that laser structuring considerably affects the reduction of depth ratio, normal (up to 89%) and tangential (up to 82%) forces, and specific cutting energy. The specific cutting energy of laser-structured Si_3N_4 workpieces converged to about 5 J/mm³, much lower than that of unstructured workpieces.

Keywords Material removal mechanism · Laser structuring · Single diamond grit scratching, Silicon nitride (Si_3N_4) · Ultrashort-pulse laser · Specific cutting energy

1 Introduction

Besides excellent mechanical properties, silicon nitride (Si_3N_4) also has exceptional thermal properties that make it suitable for demanding industrial and medical applications comprising ball and roller bearings, heating tubes, turbocharger rotors, spark igniters, and orthopedic implants [1–4]. However, Si_3N_4 , as an advanced ceramic, is difficult to cut material due to its elevated strength, hardness, corrosion resistance, and fracture toughness. Grinding with diamond tools is the primary machining process of Si_3N_4 and other hard and brittle materials. However, efficient grinding of these materials is countered by high cutting forces

and temperature, tool wear, and generally reduced workpiece quality due to the brittle material removal regime [5]. Accordingly, despite the superior material properties of advanced ceramics, the use of these materials in the industry is mainly limited by the high machining costs and the mentioned technical constraints. According to the definition of precise machining, the dimensional and geometrical accuracy should be at least two orders of magnitude below the characteristic length of the component [6]. Meeting this requirement in the grinding and micro-grinding of hard materials leads to the challenge of restricting the dimensional accuracy and the size of thermally and mechanically influenced surface zones well below the limit values required by conventional grinding.

The brittle material removal regime, as the dominant material removal mechanism in abrasive machining of hard and brittle materials, differs significantly from the well-known ductile removal regime. The brittle material removal generally causes breakouts and micro-cracks formation on

✉ Masih Paknejad
pakm@hs-furtwangen.de

¹ Institute of Precision Machining (KSF), Furtwangen University of Applied Sciences, Katharinenstr. 2, 78532 Tuttlingen, Germany

the workpiece surface [5, 7]. The laser structuring on the brittle material would enhance the material removal rate and grinding efficiency by propagating the lateral cracks [8]. The induced micro-cracks on the workpiece surface and in the subsurface of the workpiece cause significant strength reduction and substantial loss of tolerable stresses of the workpiece [5, 9–11]. Hence, in the case of Si_3N_4 and other hard and brittle materials, the surface integrity of the ground workpiece plays a crucial role in the performance, wear, and fatigue life of the workpiece [5].

It is shown that the quality loss of brittle workpieces such as advanced ceramics caused by induced subsurface damages through the brittle grinding regime could be overcome by material removal in a dominant ductile mode. The ductile grinding mode generates chips via plastic deformation rather than fracture [12]. The threshold between the ductile and brittle material removal regimes and hence the threshold for the lateral cracks' initiation into the workpiece due to the grits' penetration is defined by the critical chip thickness of the brittle material [13, 14]. It is necessary to keep the uncut chip thickness continuously below the critical chip thickness of the brittle material in order to cut the material in ductile mode. Hence, to reduce the subsurface damages, the advanced ceramics are generally ground with a very low material removal rate, causing a low uncut chip thickness (low depth of cuts and/or feed speeds).

On the other hand, low uncut chip thicknesses exponentially increase the required grinding energy (specific grinding energy) due to the size effect [5]. Although, the high hardness of advanced ceramics also causes high specific grinding energies due to the required energy for penetrating the workpiece and cutting the materials by grits [15].

Non-conventional and hybrid machining processes are developed to reduce the cutting forces and temperature and increase the achievable material removal rate in advanced ceramics machining [5, 16]. Laser structuring of the workpiece surface combined with the grinding process is one of the recently developed non-conventional and hybrid machining processes for increasing the machining efficiency of hard-to-cut materials [17]. Long-pulse laser irradiation causes more pile-up, cracks, and thermal damage than ultrashort-pulse laser [18, 19]. In other words, ultrashort-pulse lasers such as pico- and femtosecond lasers can be employed for machining difficult-to-cut materials with superior accuracy and controllability, where the ablation mechanism of the workpiece material is mainly sublimation (cold ablation) [20]. Hence, the workpiece surface can be ablated by ultrashort-pulse lasers without significant thermal damage or with minimal and controllable subsurface damage [8]. Accordingly, laser-assisted grinding, where patterned microstructures are generated on the workpiece surface by an ultrashort-pulse laser prior to the grinding process, can significantly decrease the specific cutting energy of the cutting

process along with the structural damage and increase the machinability, removal rates, and tool life [8, 17, 21–23]. Hence, in view of the challenges mentioned above in precise machining, using ultrashort-pulse laser grinding as a hybrid machining process can be a promising solution [8, 24, 25].

The single diamond grit scratching test is an approach that replicates the kinematic and dynamic of the grinding process and is widely employed to investigate the material removal mechanism of hard and brittle materials [26–33]. Researchers also employed single grit scratching to predict the grinding forces, calculate, and model the specific grinding energy of hard and brittle materials [34–39]. Therefore, understanding the single grit scratching on the material workpiece is vital to model the overall grinding process by integrating the numerous actions performed by single grit. Single diamond grit is generally mounted on the periphery of a rotating wheel body and scratches against the workpiece surface, which is fixed on the machine table. Single tracks or grooves are scratched with various depths of cuts.

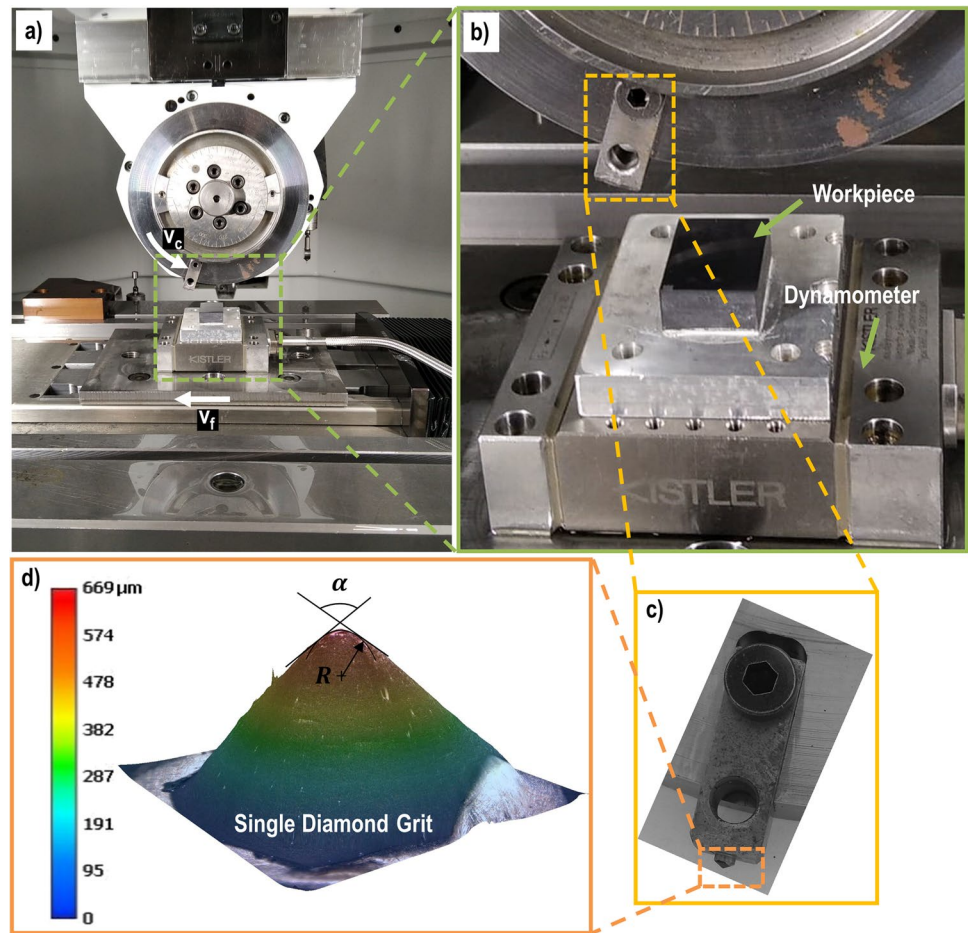
Structuring workpiece surfaces by an ultrashort-pulse laser prior to the grinding process affects the specific grinding energy and may alter the critical chip thickness of the material and hence the dominant material removal mechanism. These effects are partially due to controllable induced damages into the subsurface of the structured workpieces. However, the impacts of this surface structuring technique on the material removal mechanism of advanced ceramics such as Si_3N_4 are not yet thoroughly investigated. In this paper, single diamond grit scratching has been performed to examine the material removal mechanisms of laser-structured Si_3N_4 fundamentally. The scratching forces and the morphologies of scratch grooves have been measured and analyzed. The effects of cutting speed and undeformed chip thickness on pile-up area, area and width of the grooves, depth ratio, normal and tangential forces, and specific scratching energy have been explored on non-structured and laser-structured surfaces.

2 Experimental setup and procedures

Figure 1 illustrates the experimental setup, including the workpiece, a piezo multi-component dynamometer (Kistler type 9256C), and a single diamond grit with a defined geometry. The tip radius (R) and angle of single grit (α) are 215 μm and 120°, respectively. This single grit was brazed to a rod mounted on the perimeter of a disk. The distance between the grit's tip and the disk's center was 84 mm. It means that the rotation diameter (d_s) is 168 mm. The experiments were carried out on a 5-axis grinding center Haas Multigrind® CA.

Gas pressure-sintered silicon nitride (GPSSN) was selected as the workpiece material. The thermomechanical

Fig. 1 (a) Experimental setup. (b) Magnified view of the experimental setup. (c) Magnified view of single diamond grit and related fixture. (d) Single diamond grit with a defined geometry (tip radius (R) of 215 μm and tip angle (α) of 120°)



properties of the workpiece material are mentioned in Table 1. Block samples with dimensions of $30 \times 20 \times 10$ mm were ground and polished, and the surface roughness (R_a) of about 0.13 μm was induced on the surface of the specimens. Before the single grit scratching, the workpiece surface was structured with two different laser percentages, 25% and 50%, by a CNC-laser machine (GF Femto Flexipulse Laser P 400 U). The workpiece was irradiated with a femtosecond Yb:YAG laser with a wavelength of 1030 nm, a beam diameter (d_B) of 40 μm , a pulse duration of 250 fs, a pulse frequency of 400 kHz, a focal length of 70 mm, an average power of 40 W, and a scanning speed of 2 m/s. The laser structuring pitches were 100 μm and 50 μm for 25% and 50% (Fig. 2) laser structuring, respectively. Moreover, the wall thicknesses between the microstructures were 75 μm and

25 μm for 25% and 50% laser structuring (Fig. 3). The laser-structured depth is about 20 μm for both laser-structured samples.

The single grit scratching tests were carried out at different depths of cuts ($h_{cu\max}$) within three cutting speeds (v_c) 4, 8, and 10 m/s, and a constant feed rate (v_f) of 5 m/min. The tests were carried out in the dry condition and up-grinding mode, where the grit traveled up the workpiece in the opposite direction of the table movement. Also, the direction of scratching tests for the laser-structured samples was perpendicular to the structured surface. The 3D topology and characteristics of scratch grooves, including the groove's depth, width, and length, the pile-up, and the material removed volume, have been measured by a confocal microscope (Nanofocus Mobile μsurf) and analyzed by μsoft analysis premium 7.2 and MATLAB software.

Table 1 Thermomechanical properties of GPS Si_3N_4 [39]

Elastic modulus	Density	Specific heat capacity	Thermal conductivity	Decomposition temperature	Vickers microhardness	Fracture toughness, K_{IC}
(GPa)	(kg/m^3)	(J/kgK)	(W/mK)	(°C)	(HV1)	($\text{MPa}\cdot\text{m}^{1/2}$)
310	3210	700	21	1300	1650	7

Fig. 2 Polished samples. (a) Non-structured sample. (b) 50% laser-structured sample (laser parameters: $v_L = 2$ m/s, $P_L = 40$ W, $t_{\text{pulse}} = 250$ fs)

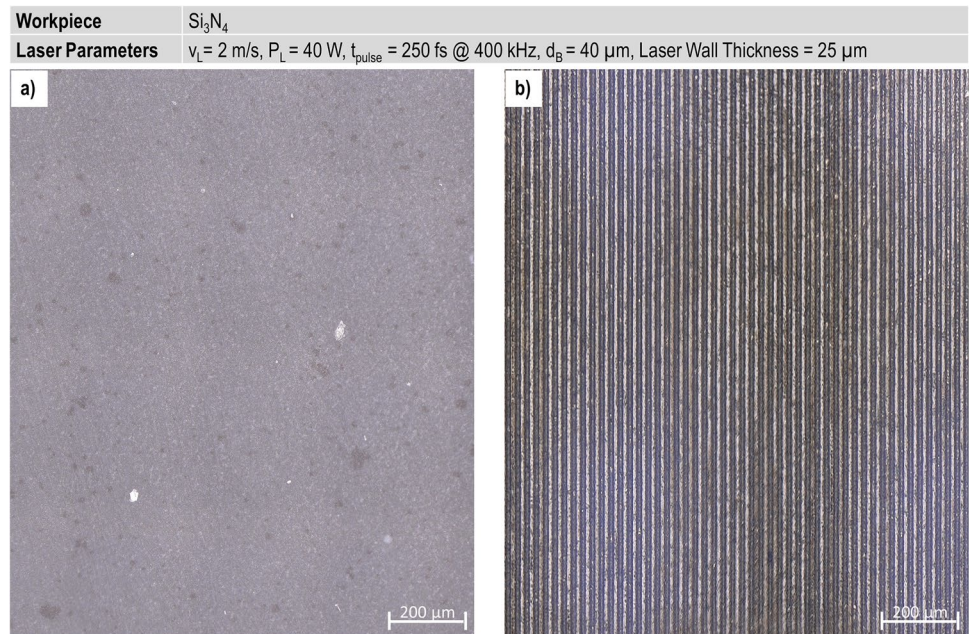
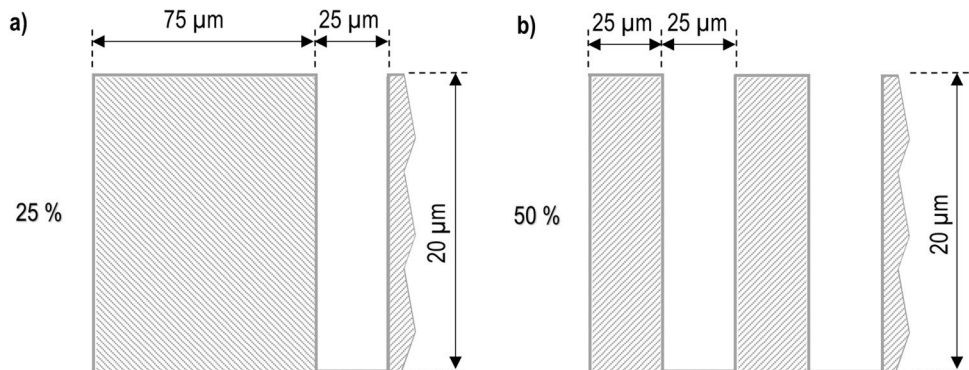


Fig. 3 Schematic laser-structured surfaces at (a) 25% and (b) 50% laser structuring



The 3D views of the single grit scratch on non-structured and laser-structured samples are shown in Fig. 4. Area of grooves and pile-up were obtained using MATLAB code by finding the most profound section in the grit path in the images analyzed by the μsoft analysis software from the confocal microscopy. As the actual and theoretical scratch depths might be different owing to the elastic deformations of the machining setup and environmentally induced uncertainties, the measurement of the scratch path length on the captured 3D images, as shown in Fig. 4, is used to evaluate the actual depth of cut values corresponding to the individual cutting path lengths.

3 Results and discussion

3.1 Area of groove and pile-up

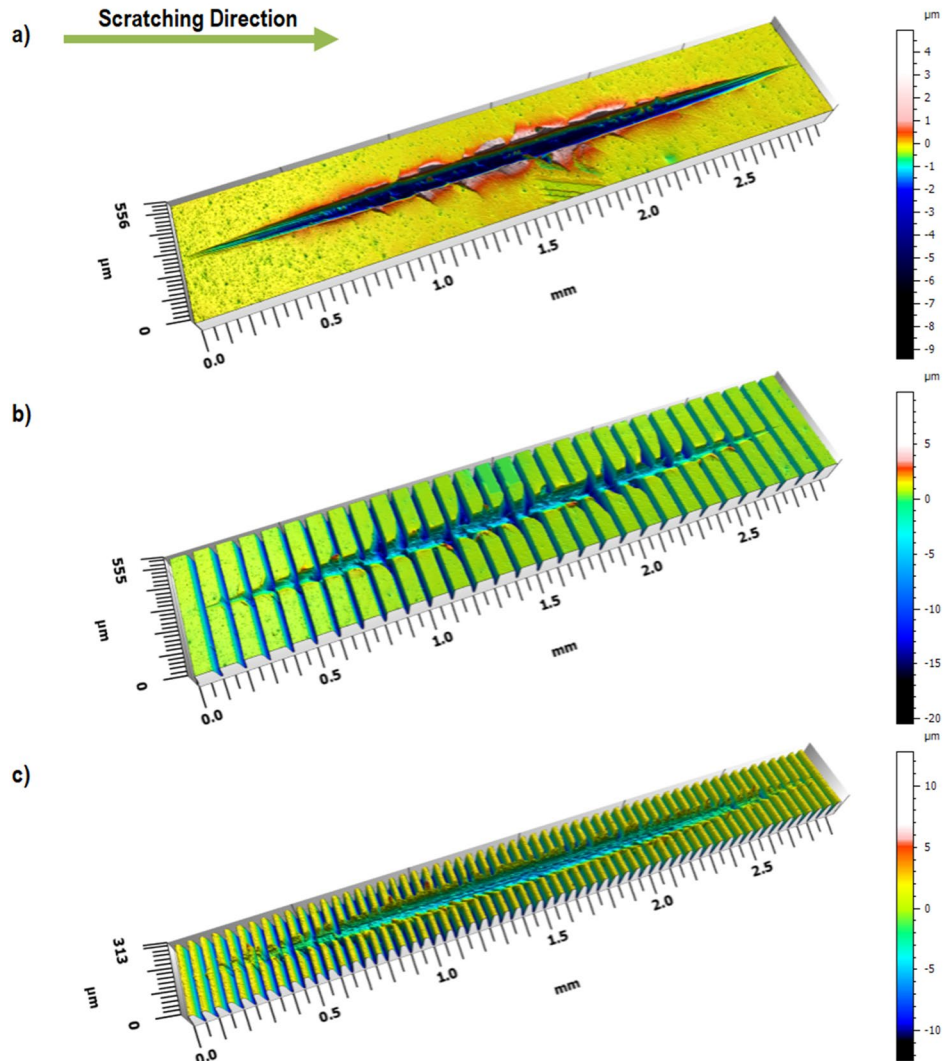
The effects of the maximum depth of cut ($h_{\text{cu max}}$) on the groove and pile-up areas and the width of scratches in the

deepest section for three cutting speed levels (4, 8, and 10 m/s) are shown in Fig. 5 for non-structured surfaces. As shown in Figs. 5 and 6, the groove and pile-up area and the groove width rise with scratch depth ($h_{\text{cu max}}$) independent of the utilized cutting speed. Hence, rising the material removal rate causes higher groove areas. Generally, in brittle materials such as Si_3N_4 , the pile-up area around the scratched groove is caused by the lateral microcracks in the subsurface region of the groove [26, 41]. The number and length of the lateral microcracks increased with the undeformed chip thickness, increasing the acting stress on the workpiece surface.

Figures 7 and 8, which correspond to the deepest section of the scratches, show that the remaining pile-up area and the width of the groove are, respectively, reduced and increased by increasing the cutting speed. The reduction of the remaining pile-up area lies in the fact that the supporting area for the pile-up formation was diminished owing to the expansion of the groove width in direct correspondence

Fig. 4 Single grit scratches. (a) Non-structured surface. (b) 25% laser-structured surface. (c) 50% laser-structured surface

Cutting Tool	Single Diamond Grit, Tip Radius = 215 μm , Tip Angle = 120 $^\circ$
Workpiece	Si_3N_4
Cutting Parameters	$v_c = 8 \text{ m/s}$, $v_f = 5 \text{ m/min}$, $h_{\text{cu max}} = 13 \mu\text{m}$, $d_s = 168 \text{ mm}$
Laser Parameters	$v_L = 2 \text{ m/s}$, $P_L = 40 \text{ W}$, $t_{\text{pulse}} = 250 \text{ fs @ } 400 \text{ kHz}$, $d_B = 40 \mu\text{m}$, Laser Wall Thickness = 25, 75 μm



with the cutting speed. The impact force of the diamond grit on the workpiece surface rises with the cutting speed, increasing the microcrack growth in axial and lateral directions [26]. The initiation and propagation of microcracks cause more chipping along the width of the scratch (Fig. 9) and may even lead to material removal beneath the actual grit path. Although more pile-up area could be expected by increasing the lateral microcracks, the supporting surface of the pile-up was removed by the chipping of the groove walls, causing an increase in the groove width (Fig. 6). The deviant point in Figs. 5 and 6 for the process condition of feed speed, $v_f = 5 \text{ m/min}$, cutting speed, $v_c = 10 \text{ m/s}$, and maximum depth of cut, $h_{\text{cu max}} = 13 \mu\text{m}$ is an indication of the occurrence of significant chipping or fragmentation which cause a remarkable increase in the area and width of the groove

and a notable reduction in the pile-up area. Accordingly, Figs. 7(c) and 8(c) illustrate the increment of groove cross-sectional area at the highest cutting speed of $v_c = 10 \text{ m/s}$. Furthermore, the deviant point in Fig. 5 for the process condition of feed speed, $v_f = 5 \text{ m/min}$, cutting speed, $v_c = 4 \text{ m/s}$, and maximum depth of cut, $h_{\text{cu max}} = 13 \mu\text{m}$ verifies the considerable increase of micro-crack occurrence, which leads to noticeably larger pile-up areas. In other words, when the dominant material removal mechanism is brittle, the length and number of microcracks will be raised. Consequently, structural damage will increase even in the subsurface of hard and brittle workpiece material.

The area of groove and pile-up at the deepest sections of scratches induced at the process parameter of feed speed, $v_f = 5 \text{ m/min}$, cutting speed, $v_c = 8 \text{ m/s}$, and maximum

Fig. 5 Effects of the cutting speed (v_c) on the area of groove and pile-up at the feed rate of 5 m/min for different values of maximum depth of cut, $h_{cu\ max}$

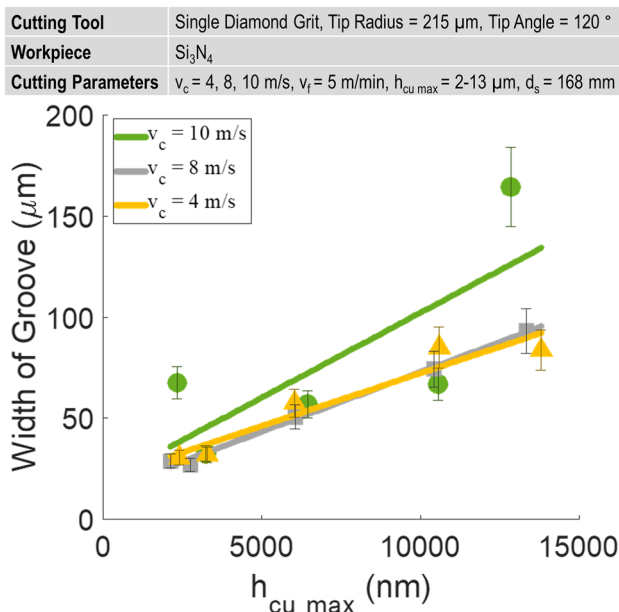
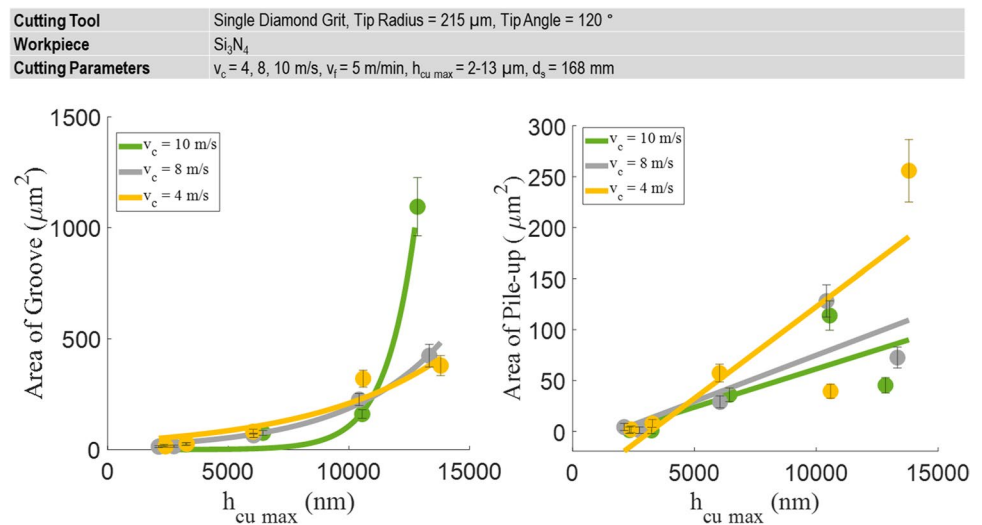


Fig. 6 Effects of the cutting speed on the groove width at the deepest sections ($h_{cu\ max}$) of various grooves

depth of cut, $h_{cu\ max} = 13\ \mu\text{m}$ on the non-structured and laser-structured samples are illustrated in Fig. 10. The groove area was increased from 424 μm^2 in the case of non-structured surface to 2397 μm^2 (465%) and 801 μm^2 (89%) for 25% and 50% laser structuring, respectively. The laser structuring of the workpiece caused intermittent cutting, which resulted in a series of impacts during the scratching procedure. With a significant increase in the groove area, the interrupted cutting could promote the initiation and propagation of lateral and axial microcracks [42, 43] (Fig. 11). A higher percentage of laser structuring leads to an increase in the effects of intermittent impacts.

However, an excessive wall thickness reduction due to a greater extent of surface structuring could set a barrier to the growth of lateral cracks. Accordingly, the amount of structural damage decreases with the percentage of the laser-structured surface, limiting the rise in groove area and decreasing the groove width (Fig. 10 and Fig. 12).

The effect of wall thickness on crack propagation has been shown in Fig. 9. While the wall thickness is large enough (Fig. 9b), the lateral crack propagation is more efficient, and consequently, the structural damage and the chip formation efficiency increase.

The pile-up area decreased wherever the impact force increased, whether this impact force was due to an increase in the cutting speed (Fig. 7) or due to the intermittent cutting by laser structuring (Figs. 10 and 11). As shown in Fig. 9, the chipping will occur during the scratching so that the number and volume of these fragmentations directly increase by increasing the percentage of laser structure (increasing the number of intermittent occurrences) and increasing the wall thickness of the laser structures. Furthermore, successive elastic deformation and recovery of the diamond grit increase due to more intermittent occurrences, and consequently, the actual depth of cut rises; therefore, more structural damage will happen. In the case of intermittent cutting on the laser-structured surfaces, more evidence of brittle fracture can be observed in the form of lateral and radial cracks, which contribute to the material chipping and fragmentation. As shown in Fig. 9, along each scratch path, the length of cracks or the sizes of the fragmentations are not directly related to the depth of cut; besides the nonregular nature of the brittle removal mechanism, this deviation would be due to the inhomogeneity, structural defects, and anisotropy of the hard and brittle workpiece material.

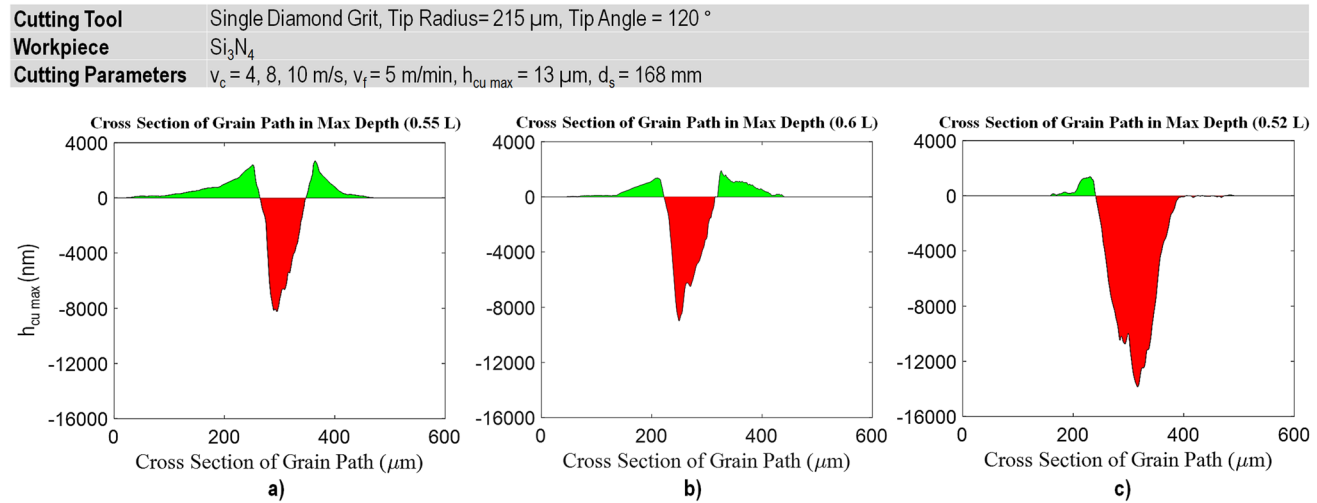
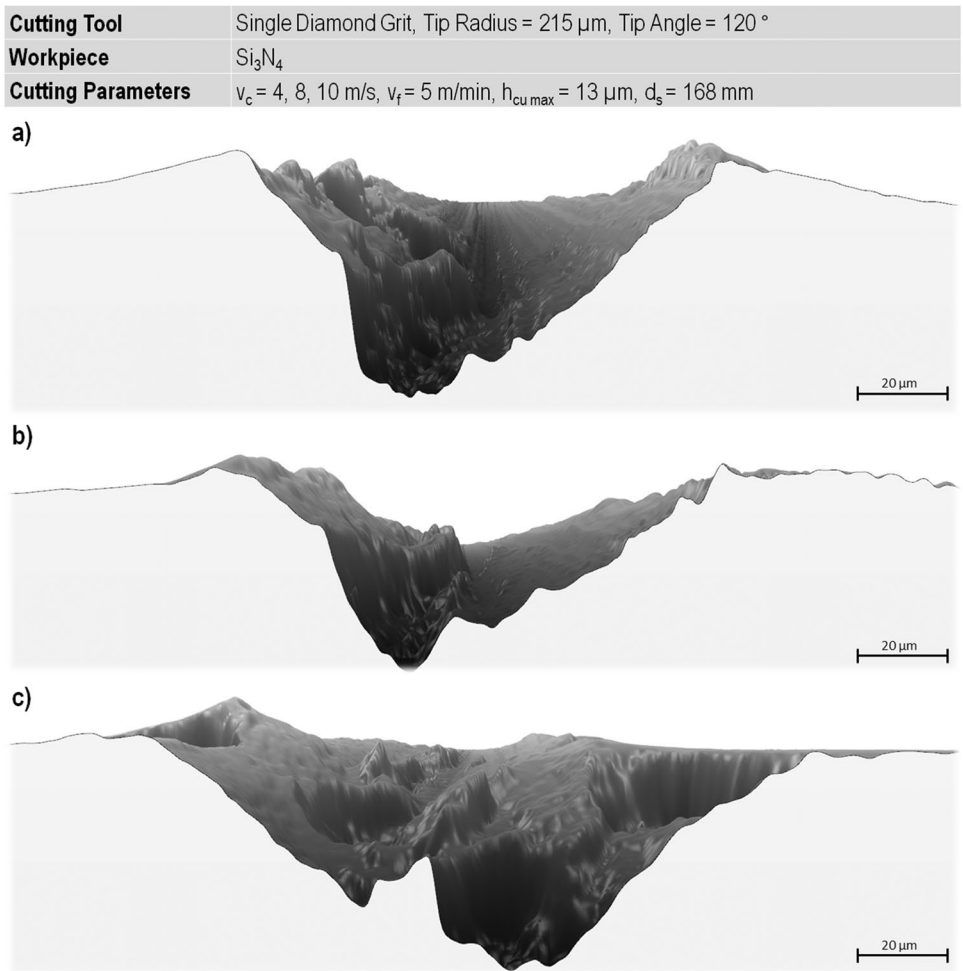


Fig. 7 Area of groove and pile-up at the deepest section of the scratches ($h_{\text{cu max}} = 13 \mu\text{m}$) induced at various cutting speeds on non-structured surface. **(a)** $v_c = 4 \text{ m/s}$. **(b)** $v_c = 8 \text{ m/s}$. **(c)** $v_c = 10 \text{ m/s}$

Fig. 8 Section view at the deepest section of the scratches ($h_{\text{cu max}} = 13 \mu\text{m}$) induced at various cutting speeds on non-structured surface. **(a)** $v_c = 4 \text{ m/s}$. **(b)** $v_c = 8 \text{ m/s}$. **(c)** $v_c = 10 \text{ m/s}$



Cutting Tool	Single Diamond Grit, Tip Radius = 215 μm , Tip Angle = 120 °
Workpiece	Si_3N_4
Cutting Parameters	$v_c = 8 \text{ m/s}$, $v_f = 5 \text{ m/min}$, $h_{cu \text{ max}} = 13 \text{ }\mu\text{m}$, $d_s = 168 \text{ mm}$
Laser Parameters	$v_L = 2 \text{ m/s}$, $P_L = 40 \text{ W}$, $t_{\text{pulse}} = 250 \text{ fs @ } 400 \text{ kHz}$, $d_B = 40 \text{ }\mu\text{m}$, Laser Wall Thickness = 25, 75 μm

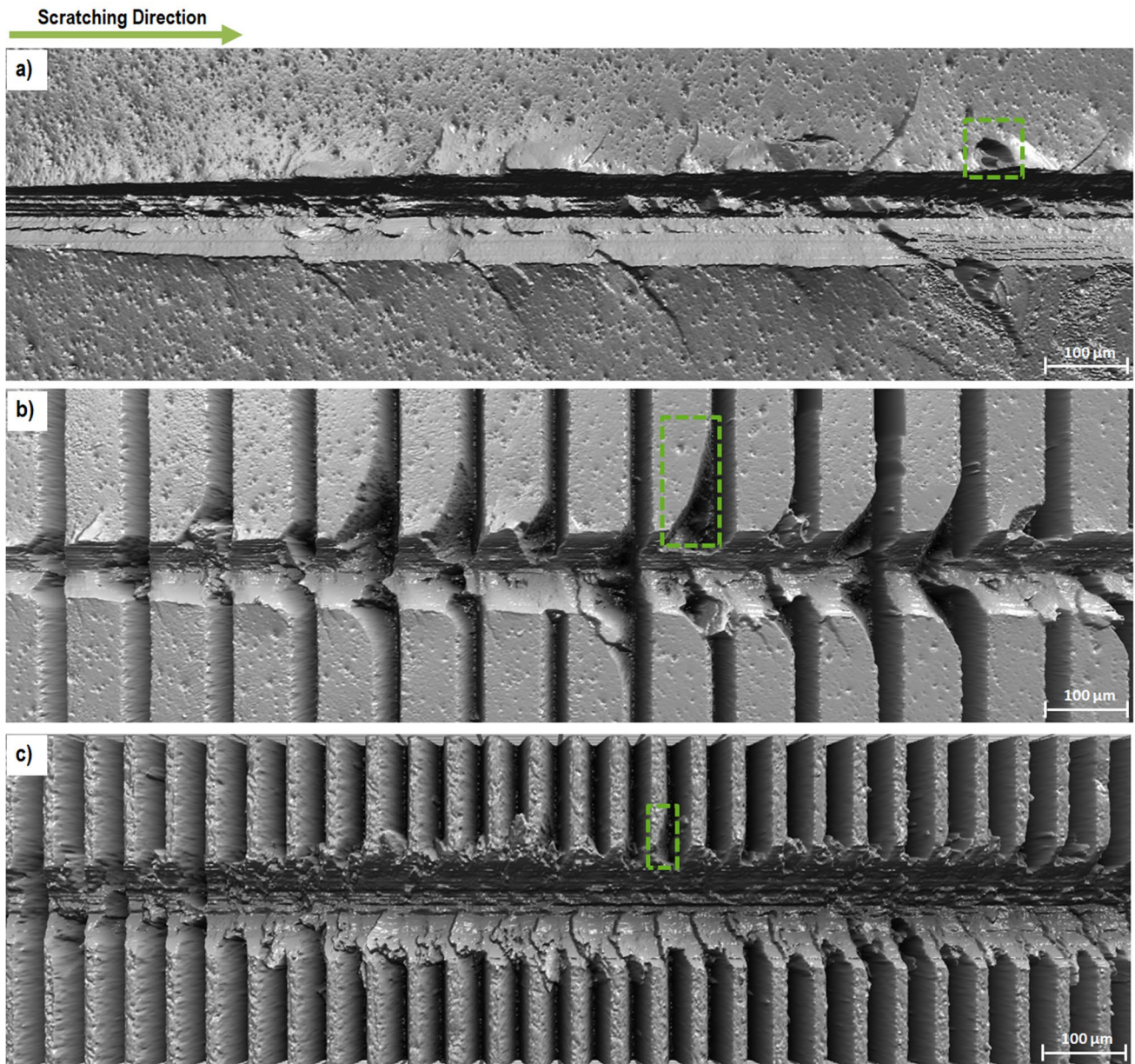


Fig. 9 Effect of laser structure and wall thickness on crack propagation and chipping along the width of scratch. (a) Non-structured surface. (b) 25% laser-structured surface. (c) 50% laser-structured surface

Cutting Tool	Single Diamond Grit, Tip Radius = 215 μm , Tip Angle = 120 °
Workpiece	Si_3N_4
Cutting Parameters	$v_c = 8 \text{ m/s}$, $v_f = 5 \text{ m/min}$, $h_{\text{cu max}} = 13 \mu\text{m}$, $d_s = 168 \text{ mm}$
Laser Parameters	$v_L = 2 \text{ m/s}$, $P_L = 40 \text{ W}$, $t_{\text{pulse}} = 250 \text{ fs @ } 400 \text{ kHz}$, $d_B = 40 \mu\text{m}$, Laser Wall Thickness = 25, 75 μm

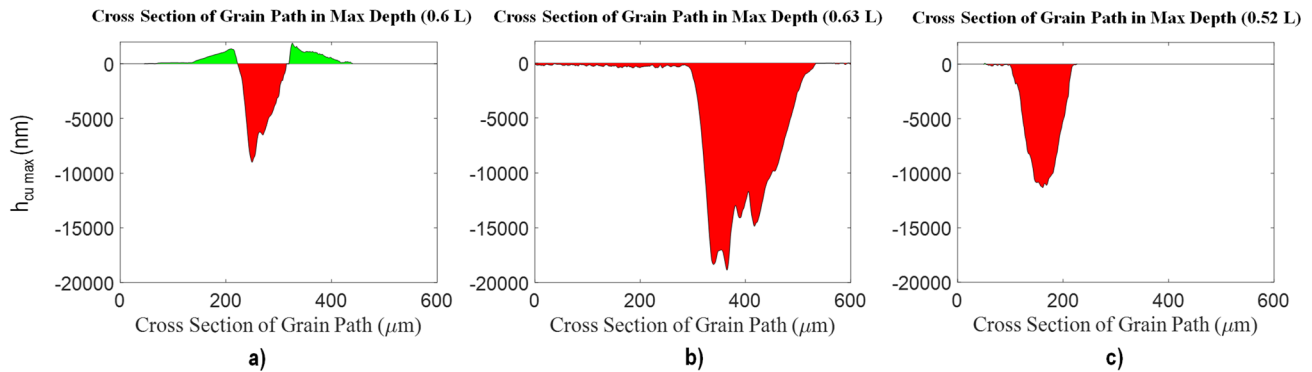
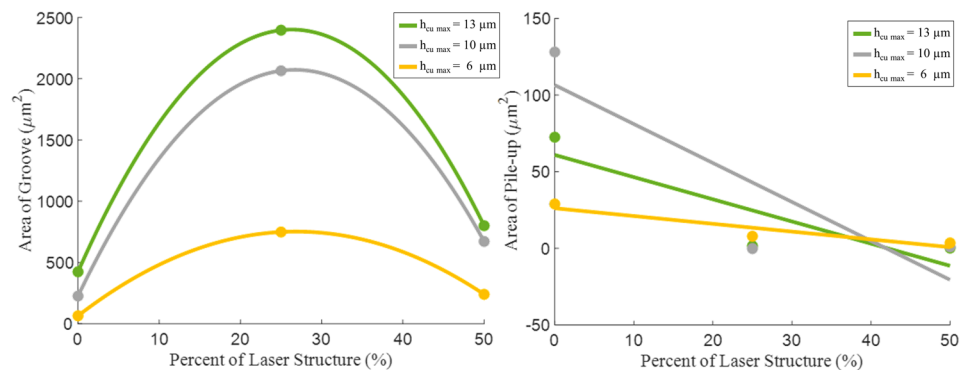


Fig. 10 Area of groove and pile-up at deepest section of the scratches at the cutting speed of 8 m/s ($h_{\text{cu max}} = 13 \mu\text{m}$). (a) Non-structured surface. (b) 25% laser-structured surface. (c) 50% laser-structured surface

Fig. 11 Effects of the workpiece laser structuring on the area of groove and pile-up at the cutting speed of 8 m/s and the feed rate of 5 m/min

Cutting Tool	Single Diamond Grit, Tip Radius = 215 μm , Tip Angle = 120 °
Workpiece	Si_3N_4
Cutting Parameters	$v_c = 8 \text{ m/s}$, $v_f = 5 \text{ m/min}$, $h_{\text{cu max}} = 6, 10, 13 \mu\text{m}$, $d_s = 168 \text{ mm}$
Laser Parameters	$v_L = 2 \text{ m/s}$, $P_L = 40 \text{ W}$, $t_{\text{pulse}} = 250 \text{ fs @ } 400 \text{ kHz}$, $d_B = 40 \mu\text{m}$, Laser Wall Thickness = 25, 75 μm



3.2 Single grit path

The theoretical path of single diamond grit, scratching the workpiece surface, could be calculated according to the below equation:

$$h_{\text{cu max}} = R - R \cos \theta \quad (1)$$

$$\theta = \sin^{-1} \left(\frac{L}{2R} \right) \quad (2)$$

where R , θ , and L are the distance from the single grit to the center of the rotating disk, half path angle, and projected path length, respectively (Fig. 13).

The generated paths by the single diamond grit scratching experiments on non-structured and 25% and 50% laser-structured surfaces at $h_{\text{cu max}} = 13 \mu\text{m}$, $v_c = 8 \text{ m/s}$, and $v_f = 5 \text{ m/min}$ are shown in Fig. 14. The theoretical path of the single diamond grit on the workpiece surface is plotted by fitting a circle to three points of the path, including the first point and endpoint of the path, which is measured by a confocal microscope and the theoretical $h_{\text{cu max}}$. As shown in Fig. 14, for non-structured surfaces, the experimental real grit path lies significantly above the theoretical path. Only in the case of laser-structured surfaces, the experimental and the theoretical paths approach each other. The path followed

Cutting Tool	Single Diamond Grit, Tip Radius = 215 μm , Tip Angle = 120°
Workpiece	Si_3N_4
Cutting Parameters	$v_c = 8 \text{ m/s}$, $v_f = 5 \text{ m/min}$, $h_{cu \text{ max}} = 6, 10, 13 \mu\text{m}$, $d_s = 168 \text{ mm}$
Laser Parameters	$v_L = 2 \text{ m/s}$, $P_L = 40 \text{ W}$, $t_{\text{pulse}} = 250 \text{ fs}$ @ 400 kHz, $d_B = 40 \mu\text{m}$

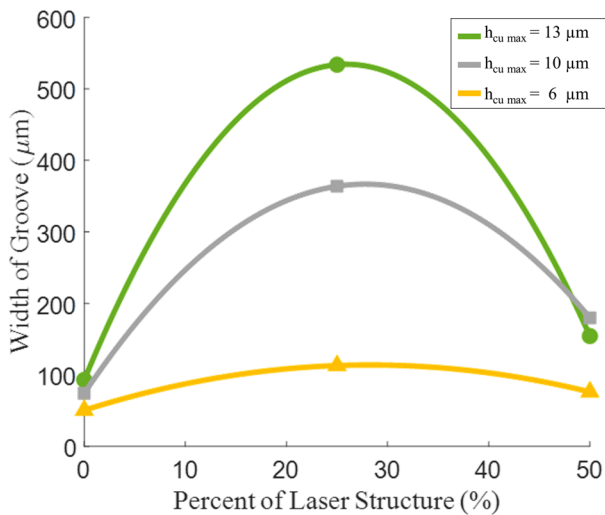


Fig. 12 Effects of the workpiece laser structuring on the groove width at the deepest sections

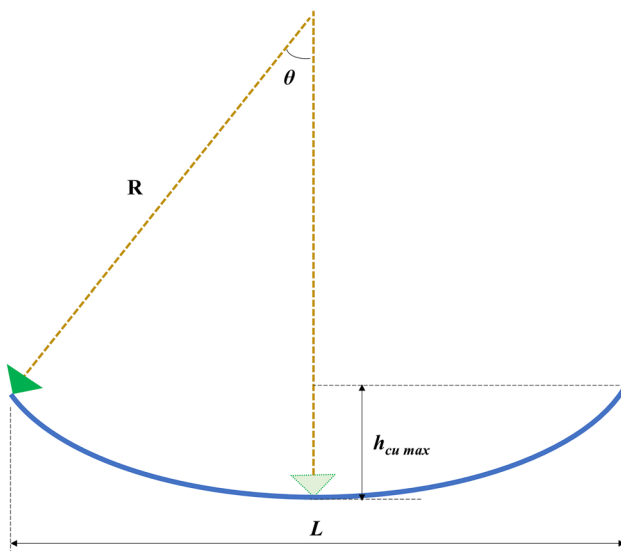


Fig. 13 Schematic of a single grit path

by the diamond grit on laser-structured surfaces is even deeper than the theoretical path. The larger grit penetration depth on laser-structured surfaces could be due to the earlier onset of the brittle material removal regime, where the initiation and propagation of micro cracks and, consequently, macro cracks will be more and cause more structural damage. Accordingly, the depth ratio is defined in Eq. 3 and plotted in Fig. 15 to evaluate the differences

between scratches produced on non-structured and laser-structured surfaces.

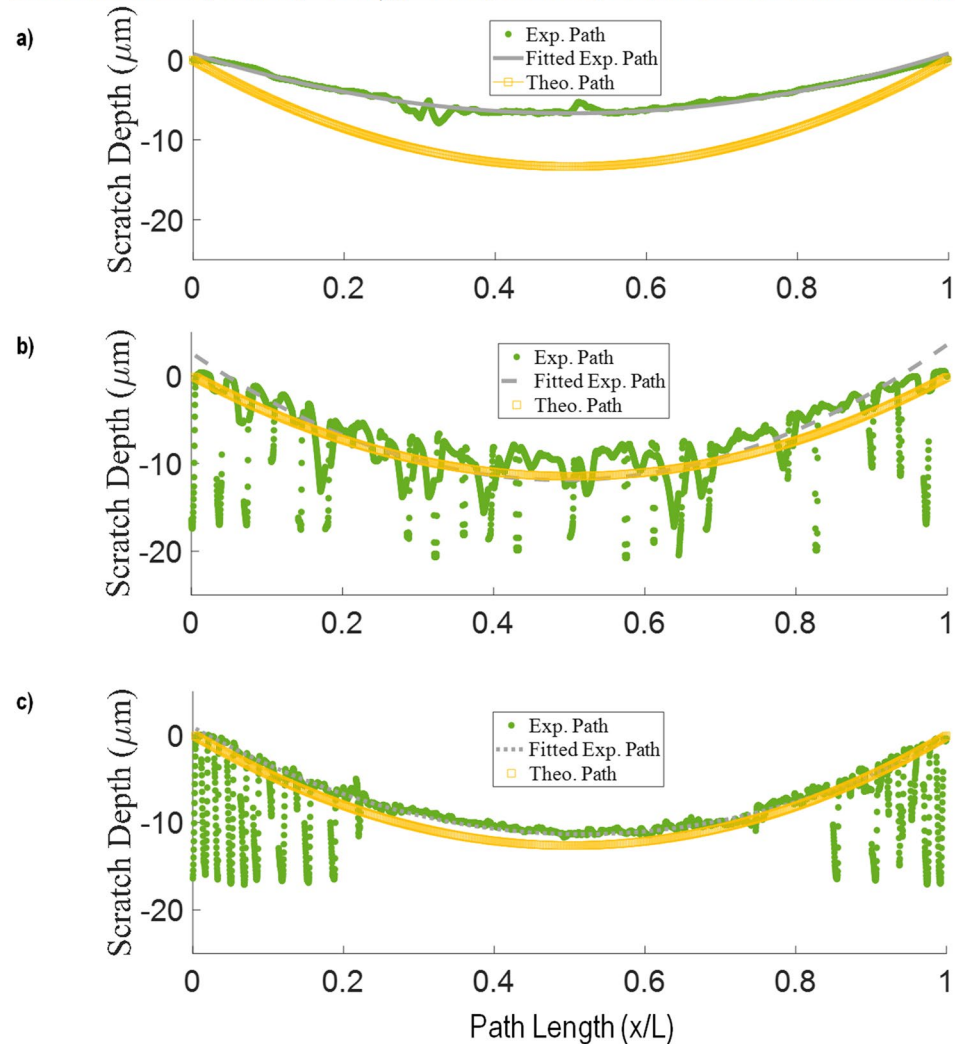
$$\text{Depth Ratio} = \frac{h_{\text{cumaxTheo}} - h_{\text{cumaxExp}}}{h_{\text{cumaxTheo}}} \quad (3)$$

As depicted in Fig. 15, in non-structured surfaces, the depth ratio decreases while the depth of cut increases, which is due to the fact that the contribution of elastic deformation is smaller, and the propagation of radial cracks is more pronounced in larger cutting depth values. Furthermore, the reduction of depth ratio is more significant at lower cutting speeds, resulting from less elastic deformation and sufficient cutting time. In other words, while the depth of cut increases, the effects of elastic backlash, spring back, unbalancing of disk carrying the single grit, out of flatness, and also the roughness value of workpiece will be more negligible in microscale and consequently, the experimental grit path converges more to the theoretical path.

The depth ratio was much lower for laser-structured surfaces compared to non-structured surfaces. This reduction may be due to the intermittent cutting, which decreases the effect of spring back, elastic deformation, and cutting forces (compare Fig. 19). The material weakening owing to the laser-structuring also contributes to the decrement of cutting forces and elastic deformation of the diamond grit and the workpiece. Additionally, the single diamond grit follows the theoretical path during each laser structure period (since there is no contact between the grit and the workpiece surface in this period). Accordingly, the subsequent engagement of the diamond grit with the workpiece occurs at a depth corresponding to the theoretical path. Moreover, the impact forces due to this intermittent cutting can initiate and propagate microcracks on the walls of the structures, leading to a weakening of the material in such a way that, in some cases, the depth ratio changes to minus values. Negative depth ratio values indicate that the actual material removal is extended beyond the limit defined by the theoretical grit path. This negative ratio could be due to the domino effect of crack propagation and secondary chipping that amplify the effect of intermittent phenomena in laser structure surfaces. However, the depth ratio increased with the depth of cut in the case of laser-structured samples. As presented in Fig. 16, the increase in depth ratio at higher depths of cuts is due to the geometrical characteristic of laser structures, which makes it impossible to generate perfectly vertical structure walls. Therefore, the structure thickness increases, and the effect of laser structuring on the material removal decreases. Furthermore, the concentration of laser-induced damage in the vicinity of the laser structures and their contribution to the chip removal reduce (Fig. 16) at higher depths of cut.

Fig. 14 Experimental and theoretical grit paths (a) on the non-structured surface, (b) on 25% laser-structured surface, and (c) on 50% laser-structured surface

Cutting Tool	Single Diamond Grit, Tip Radius = 215 μm , Tip Angle = 120 $^\circ$
Workpiece	Si_3N_4
Cutting Parameters	$v_c = 8 \text{ m/s}$, $v_f = 5 \text{ m/min}$, $h_{cu \text{ max}} = 13 \mu\text{m}$, $d_s = 168 \text{ mm}$
Laser Parameters	$v_L = 2 \text{ m/s}$, $P_L = 40 \text{ W}$, $t_{\text{pulse}} = 250 \text{ fs @ } 400 \text{ kHz}$, $d_B = 40 \mu\text{m}$, Laser Wall Thickness = 25, 75 μm



3.3 Lateral crack propagation

While the single diamond grit scratches the workpiece surface, the stress in the front end of the grit is mainly compressive, and the stress in the plastic removal zone is tensile. The lateral cracks propagate along the direction of the maximum stress gradient, which is in the oblique front of the grit [26, 44]. Accordingly, Figs. 17 and 18 confirm that on both non-structured and laser-structured surfaces, the lateral cracks were generated oblique to the groove direction, and the number and the length of these cracks increased with the depth of cut. On the laser-structured surfaces, the generated lateral cracks mainly cause chipping and fragmentation, which could be due to the lack of bulk material to absorb the crack propagation energy and support the weakened wall.

3.4 Normal and tangential forces

The effect of cutting speed on normal and tangential forces of single grit scratching tests on non-structured surfaces at different $h_{cu \text{ max}}$ is presented in Fig. 19. Both normal and tangential cutting forces decreased by increasing the cutting speed, resulting from higher kinetic energies of the diamond grit and impact forces that are more likely to generate and propagate microcracks. An increase in the scratch depth or undeformed chip thickness caused higher material removal rates, raising the induced cutting forces.

The influence of laser structuring on normal and tangential cutting forces at $v_c = 8 \text{ m/s}$, $v_f = 5 \text{ m/min}$, and different $h_{cu \text{ max}}$ are plotted in Fig. 20. Both normal and tangential forces significantly are reduced compared with the scratching of non-structured surfaces, as observed in previous researches

Fig. 15 Effects of the laser structuring on the depth ratio at different $h_{cu \max}$

Cutting Tool	Single Diamond Grit, Tip Radius = 215 μm , Tip Angle = 120 °
Workpiece	Si_3N_4
Cutting Parameters	$v_c = 8 \text{ m/s}$, $v_f = 5 \text{ m/min}$, $h_{cu \max} = 6, 10, 13 \mu\text{m}$, $d_s = 168 \text{ mm}$
Laser Parameters	$v_L = 2 \text{ m/s}$, $P_L = 40 \text{ W}$, $t_{\text{pulse}} = 250 \text{ fs @ } 400 \text{ kHz}$, $d_B = 40 \mu\text{m}$

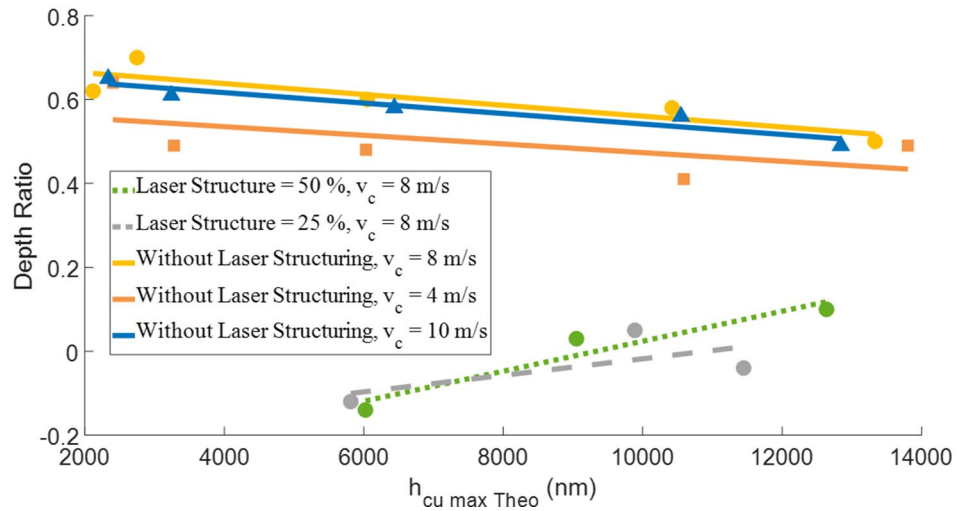
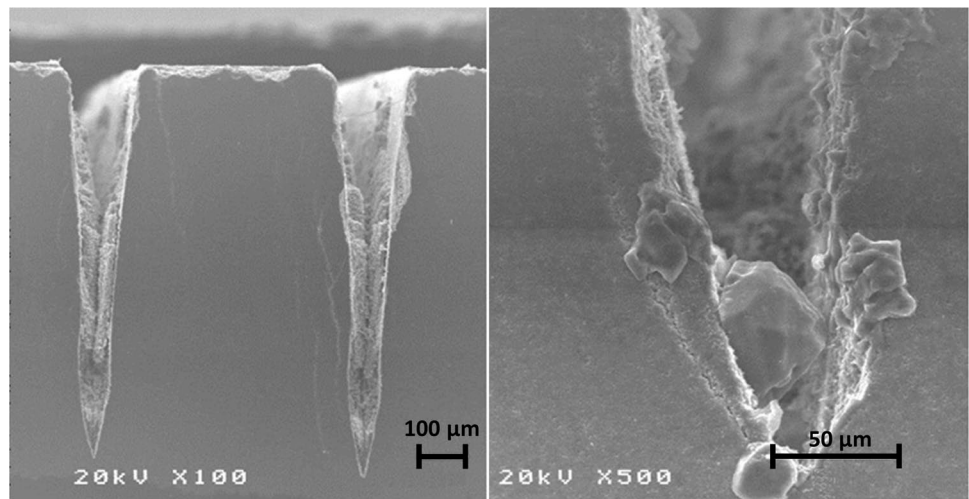


Fig. 16 Induced cracks around the structures by the laser material removal



[8, 17]. The main reasons may be related to the reduced workpiece volume, microcracks, controllable subsurface damages generated during laser structuring, and the increased impact forces due to the intermittent cutting. The reduction in cutting forces for laser-structured surfaces could be observed at all examined undeformed chip thicknesses.

3.5 Specific cutting energy

Specific cutting energy, e_c , indicates the material removal efficiency and is defined as the energy required to remove

a unit volume of material. This parameter in the single grit test is calculated as follows:

$$e_c = \frac{(v_c + v_f) \int_0^T F_t dt}{V_w} \quad (4)$$

where v_c , v_f , F_t , V_w , and T are cutting speed, feed rate, tangential force, removed material volume, and scratching test time, respectively. The plus sign in the numerator of Eq. 4 means that single grit and workpiece velocities are in opposite directions (up-grinding). In this equation, V_w is calculated by analyzing the 3D confocal images of the

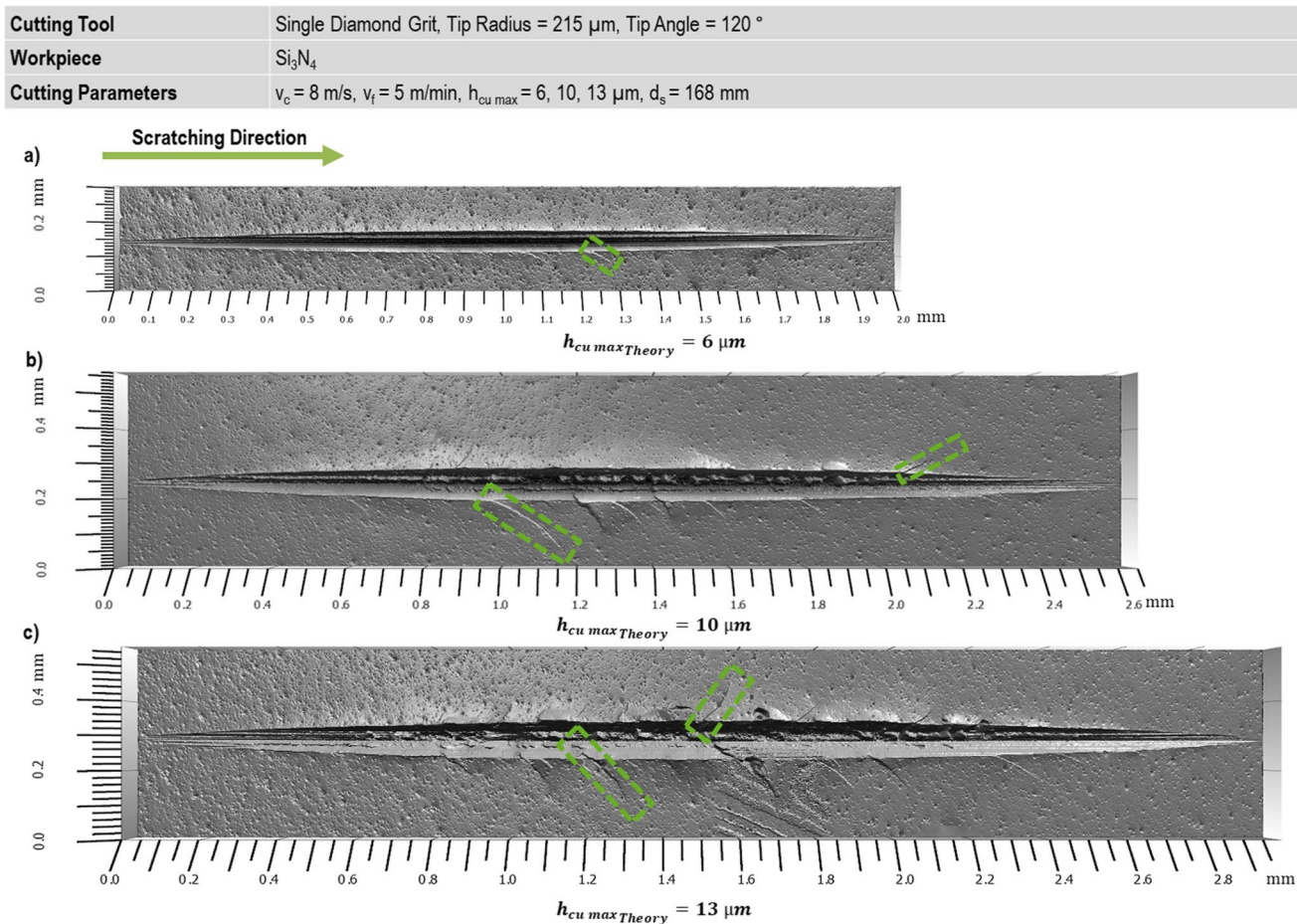


Fig. 17 Lateral crack propagation by single grit scratching on non-structured surfaces at different $h_{cu \max}$, the cutting speed of 8 m/s, and the feed rate of 5 m/min

grooves and their post-processing in MATLAB software. The area below the tangential force curve of single grit tests ($\int_0^T F_t dt$) is also calculated by evaluating the measurement data obtained by the Kistler dynamometer using MATLAB software.

The effects of cutting speed and feed rate on the specific energy of laser-structured and non-structured samples are shown in Fig. 21. In the case of non-structured surfaces, the specific energy had its highest value at low material removal volumes. Hence, most of the energy was spent on sliding and plowing instead of cutting the workpiece material, which is in accordance with the well-investigated size effect in machining. However, the specific energy tended to a constant value when the material removal volume increased, demonstrating the dominance of the cutting portion. In other words, the sliding and plowing portions in specific grinding energy will be decreased by increasing the undeformed chip thickness or material removal volume.

Interestingly, the specific energy almost did not vary at different removed material volumes for laser-structured

surfaces. Although, this constant value was lower than the lowest specific energy measured for scratching on non-structured surfaces. It appears that the sliding and plowing forces are negligible compared to the cutting forces in the case of scratching laser-structured surfaces because the specific energy is constant, and consequently, the portion of cutting is dominant. In other words, the microcracks on the walls of the structures and subsurface structural damage caused by the laser material removal [8, 17], and also the intermittent phenomena due to laser structuring and increased impact forces caused a significant reduction of specific energy at different material removal volumes.

Although cutting speed has a proportional relationship with the specific energy, it also increases the impact force of the grit, which leads to the initiation and propagation of more microcracks, and the weakening of the material. Correspondingly, the cutting forces will be reduced. The interaction of these two opposite effects finally leads to a reduction in the specific energy in sintered silicon nitride material (Fig. 21).

Cutting Tool	Single Diamond Grit, Tip Radius = 215 μm , Tip Angle = 120°
Workpiece	Si_3N_4
Cutting Parameters	$v_c = 8 \text{ m/s}$, $v_f = 5 \text{ m/min}$, $h_{cu \max} = 6, 10, 13 \mu\text{m}$, $d_s = 168 \text{ mm}$
Laser Parameters	$v_L = 2 \text{ m/s}$, $P_L = 40 \text{ W}$, $t_{\text{pulse}} = 250 \text{ fs @ } 400 \text{ kHz}$, $d_B = 40 \mu\text{m}$, Laser Wall Thickness = 75 μm

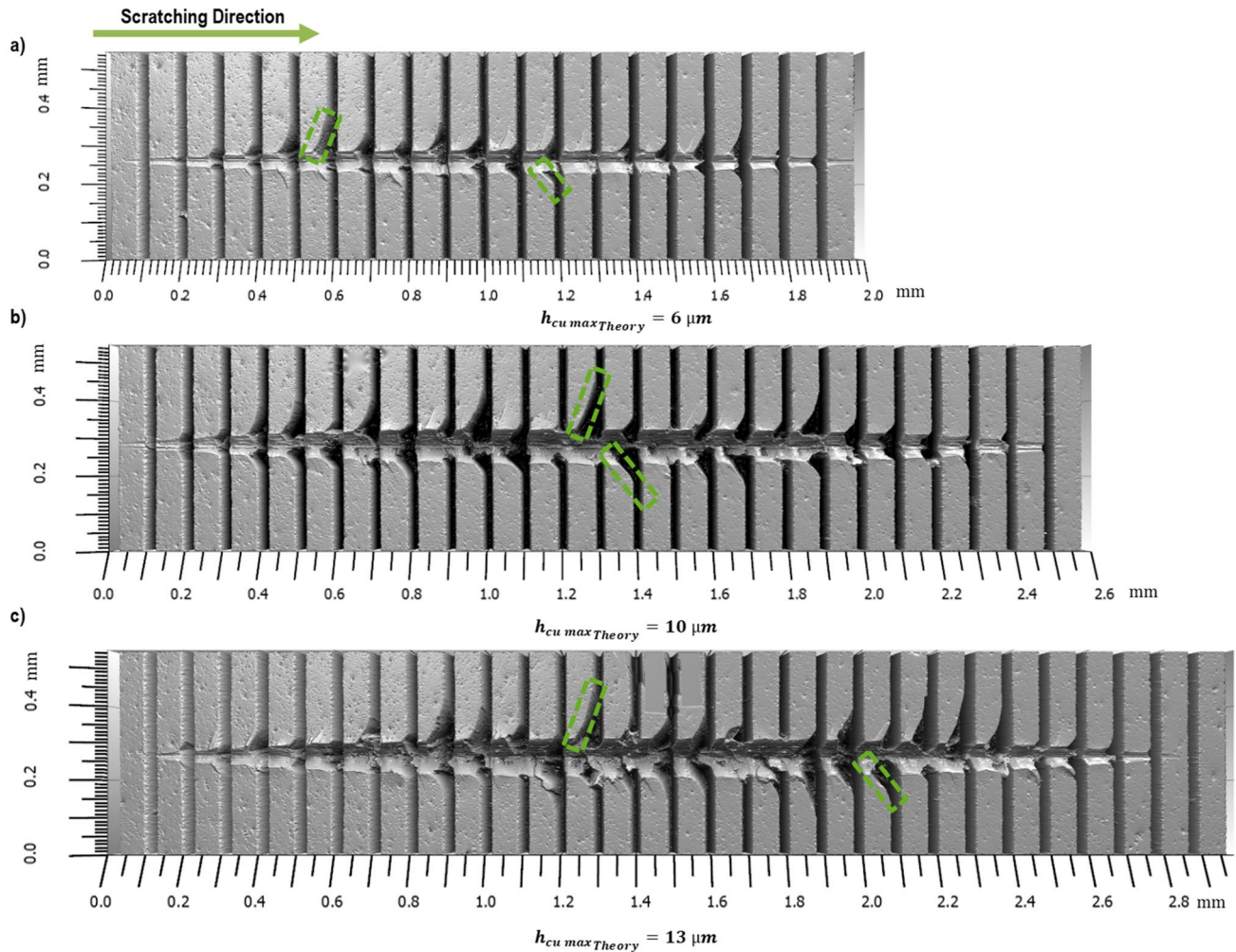


Fig. 18 Lateral crack propagation by single grit scratching on 25% laser-structured surfaces at different $h_{cu \max}$, the cutting speed of 8 m/s, and the feed rate of 5 m/min

Fig. 19 Effects of cutting speed on the normal (left) and tangential (right) cutting forces at different $h_{cu \max}$

Cutting Tool	Single Diamond Grit, Tip Radius = 215 μm , Tip Angle = 120°
Workpiece	Si_3N_4
Cutting Parameters	$v_c = 8 \text{ m/s}$, $v_f = 5 \text{ m/min}$, $h_{cu \max} = 2\text{--}13 \mu\text{m}$, $d_s = 168 \text{ mm}$

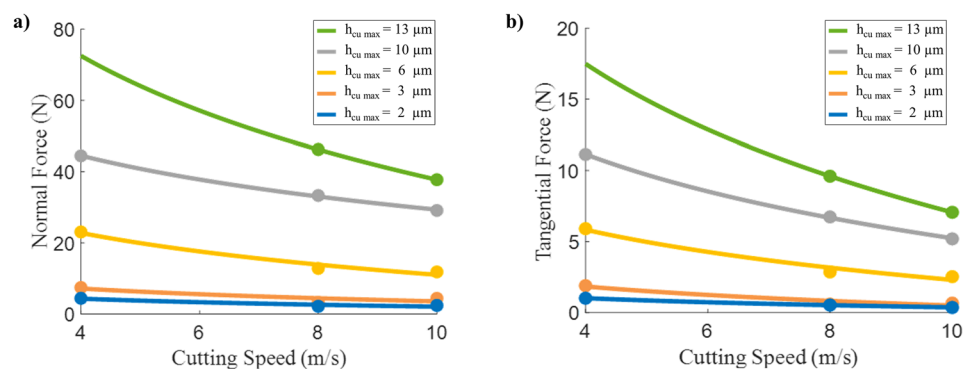


Fig. 20 Effects of the workpiece laser structuring on normal (left) and tangential (right) cutting forces at different $h_{cu \max}$

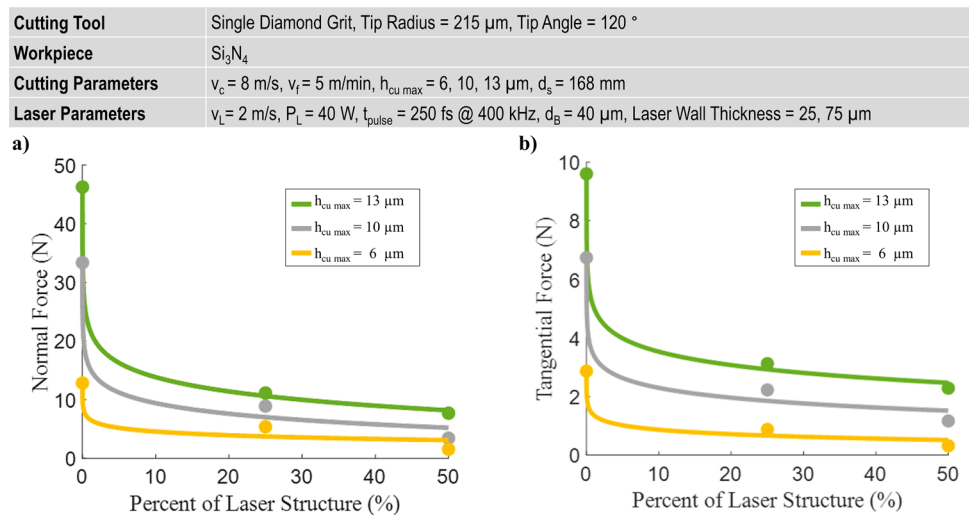
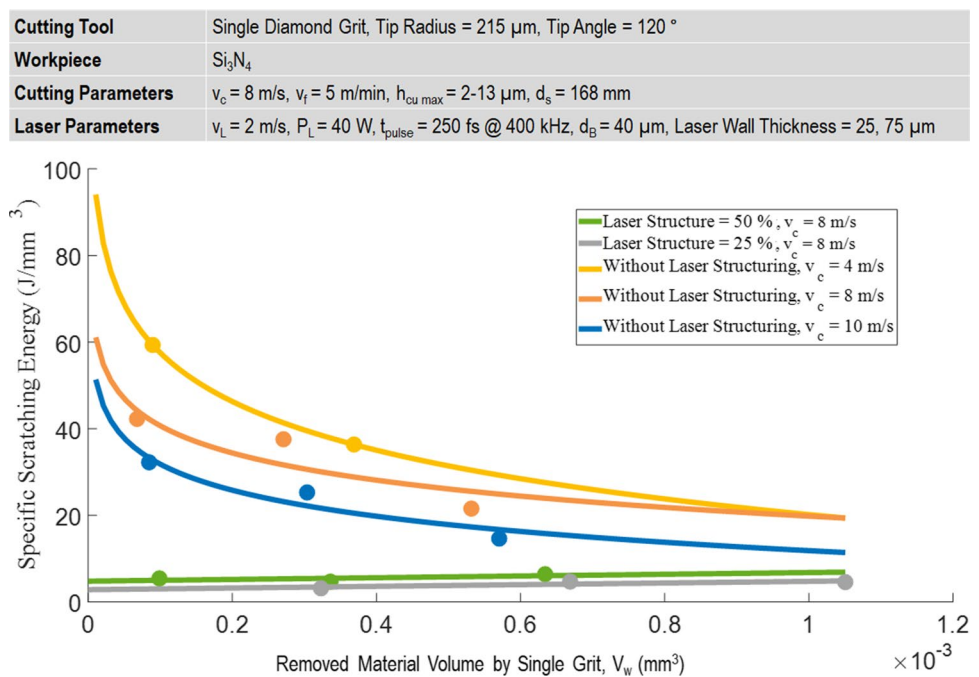


Fig. 21 Effects of the workpiece laser structuring on the specific scratching energy



4 Conclusions

The effects of ultrashort-pulse laser structuring on single diamond grit scratching of gas pressure sintered silicon nitride (GPSSN) material considering surface and subsurface damages have been experimentally investigated. The following results are concluded:

- On non-structured surfaces, the pile-up area rises along with the undeformed chip thickness. At the same time, the cutting speed has a reverse relation with the pile-up area. Furthermore, the area and width of the groove directly increase with the undeformed chip thickness.
- On laser-structured surfaces, the groove's area and width increase with increasing the undeformed chip thickness. These increment trends have an optimum value in laser-structured surfaces.
- The wall thickness of laser-structured surfaces significantly affects the grooves' area and width compared to the percentage of laser structuring.
- On non-structured surfaces, the depth ratio reduces with increasing the undeformed chip thickness. In contrast, the depth ratio converges to zero or even minus values for laser-structured surfaces.
- Both on non-structured and laser-structured surfaces, the lateral cracks onset and propagate in the oblique front of the grit.

- On non-structured surfaces, increasing cutting speed reduces normal and tangential scratching forces.
- Laser structuring surfaces cause a significant reduction in normal and tangential scratching forces.
- The specific cutting energy for laser-structured surfaces was nearly constant at different material removed volumes. In contrast, the specific energy showed an exponentially decreasing trend with removed material volume in the unstructured surfaces.
- The extension of the obtained results regarding single diamond grit to model the micro-grinding process constitutes the future of the present investigation.

Author contribution All authors contributed to the study's conception, design and analysis. Material preparation and data collection were performed by Masih Paknejad, Mohammad Ali Kadivar, and Mehdi Khakrangin. The first draft of the manuscript was written by Masih Paknejad, and all authors commented on previous versions of the manuscript. All authors read and approved the final manuscript.

Funding Open Access funding enabled and organized by Projekt DEAL. This work was supported by the German Research Foundation (DFG) (Grant Number AZ 109/2–2).

Code availability Developed MATLAB codes are available.

Data Availability Data and material are available.

Declarations

Competing interests The authors declare no competing interests.

Open Access This article is licensed under a Creative Commons Attribution 4.0 International License, which permits use, sharing, adaptation, distribution and reproduction in any medium or format, as long as you give appropriate credit to the original author(s) and the source, provide a link to the Creative Commons licence, and indicate if changes were made. The images or other third party material in this article are included in the article's Creative Commons licence, unless indicated otherwise in a credit line to the material. If material is not included in the article's Creative Commons licence and your intended use is not permitted by statutory regulation or exceeds the permitted use, you will need to obtain permission directly from the copyright holder. To view a copy of this licence, visit <http://creativecommons.org/licenses/by/4.0/>.

References

- Eichler J (2012) Industrial applications of Si-based ceramics. *J Korean Ceramic Soc* 49. <https://doi.org/10.4191/kcers.2012.49.6.561>
- Bal BS, Rahaman MN (2012) Orthopedic applications of silicon nitride ceramics. *Acta Biomater* 8:2889–2898. <https://doi.org/10.1016/j.actbio.2012.04.031>
- Supancic P, Danzer R, Harrer W et al. (2009) Strength tests on silicon nitride balls. In: *Fractography of Advanced Ceramics III*, vol 409. Trans Tech Publications Ltd, pp 193–200
- Heinrich JG, Krüner H (1994) Silicon nitride materials for engine applications. In: Hoffmann MJ, Petzow G (eds) *Tailoring of mechanical properties of Si₃N₄ ceramics*. Springer, Netherlands, Dordrecht, pp 19–41
- Bahman Azarhoushang, Ioan D. Marinescu, W. Brian Rowe et al. (eds) (2022) *Tribology and fundamentals of abrasive machining processes* (third edition), Third Edition. William Andrew Publishing
- Madou MJ (2002) *Fundamentals of microfabrication: the science of miniaturization*, second edition. Taylor & Francis
- Klocke F, Wirtz C, Mueller S et al (2016) Analysis of the material behavior of cemented carbides (WC-Co) in grinding by single grain cutting tests. *Procedia CIRP* 46:209–213. <https://doi.org/10.1016/j.procir.2016.03.209>
- Azarhoushang B, Soltani B, Daneshi A (2018) Study of the effects of laser micro structuring on grinding of silicon nitride ceramics. *CIRP Ann* 67:329–332. <https://doi.org/10.1016/j.cirp.2018.04.084>
- Jahanmir S, Ramulu M, Koshy P (1999) *Machining of ceramics and composites*. Marcel Dekker, New York
- Pfeiffer W, Hollstein T (1992) Einfluß einer Endbearbeitung auf das Festigkeitsverhalten und den Oberflächenzustand. <https://publi.ca.fraunhofer.de/handle/publica/319696>
- Pfeiffer W, Hollstein T, Zeller R (2000) Bearbeitungsbedingte Randschichtintegrität und Verschleißverhalten von Keramik. *Materialwiss Werkstofftech* 31:787–789. [https://doi.org/10.1002/1521-4052\(200008\)31:8%3c787::AID-MAWE787%3e3.0.CO;2-H](https://doi.org/10.1002/1521-4052(200008)31:8%3c787::AID-MAWE787%3e3.0.CO;2-H)
- Wu C, Li B, Liu Y et al (2017) Strain rate-sensitive analysis for grinding damage of brittle materials. *Int J Adv Manuf Technol* 89:2221–2229. <https://doi.org/10.1007/s00170-016-9237-5>
- Bifano TG, Dow TA, Scattergood RO (1991) Ductile-regime grinding: a new technology for machining brittle materials. *Journal of Engineering for Industry* 113:184–189. <https://doi.org/10.1115/1.2899676>
- Bifano TG (1988) *Ductile-regime grinding of brittle materials*. Doctoral Dissertation
- Vijayender Singh P, Venkateswara Rao S, Ghosh, (2012) Development of specific grinding energy model. *Int J Mach Tools Manuf* 60:1–13. <https://doi.org/10.1016/j.ijmachtools.2011.11.003>
- Dubey AK, Yadava V (2008) Laser beam machining—a review. *Int J Mach Tools Manuf* 48:609–628. <https://doi.org/10.1016/j.ijmachtools.2007.10.017>
- Azarhoushang B, Soltani B, Zahedi A (2017) Laser-assisted grinding of silicon nitride by picosecond laser. *Int J Adv Manuf Technol* 93:2517–2529. <https://doi.org/10.1007/s00170-017-0440-9>
- Huang H, Qian Y, Wang C et al (2020) Laser induced micro-cracking of Zr-based metallic glass using 1011 W/m² nanopulses. *Mater Today Commun* 25:101554. <https://doi.org/10.1016/j.mtcomm.2020.101554>
- Qian Y, Huang H, Wang C et al (2021) Formation of leaf-shaped microstructure on Zr-based metallic glass via nanosecond pulsed laser irradiation. *J Manuf Process* 72:61–70. <https://doi.org/10.1016/j.jmapro.2021.10.016>
- Zahedi A, Tawakoli T, Azarhoushang B et al (2015) Picosecond laser treatment of metal-bonded CBN and diamond superabrasive surfaces. *Int J Adv Manuf Technol* 76:1479–1491. <https://doi.org/10.1007/s00170-014-6383-5>
- Kadivar M, Shamray S, Soltani B et al (2019) Laser-assisted micro-grinding of Si₃N₄. *Precis Eng* 60:394–404. <https://doi.org/10.1016/j.precisioneng.2019.09.004>
- Hojati F, Azarhoushang B, Daneshi A et al (2022) Laser pre-structure-assisted micro-milling of Ti6Al4V titanium alloy. *Int J Adv Manuf Technol* 120:1765–1776. <https://doi.org/10.1007/s00170-022-08774-4>

23. Azarhoushang B, Zahedi A, Soltani B (2018) Laserunterstütztes Schleifen von Hochleistungskeramiken. In: vol 68.2018. Vulkan Verlag, Essen, pp 199–209
24. Zhang X, Wen D, Shi Z et al (2020) Grinding performance improvement of laser micro-structured silicon nitride ceramics by laser macro-structured diamond wheels. *Ceram Int* 46:795–802. <https://doi.org/10.1016/j.ceramint.2019.09.034>
25. Fortunato A, Guerrini G, Melkote SN et al (2015) A laser assisted hybrid process chain for high removal rate machining of sintered silicon nitride. *CIRP Ann* 64:189–192. <https://doi.org/10.1016/j.cirp.2015.04.033>
26. Bi Z, Tokura H, Yoshikawa M (1988) Study on surface cracking of alumina scratched by single-point diamonds. *J Mater Sci* 23:3214–3224. <https://doi.org/10.1007/BF00551297>
27. Kitzig-Frank H, Tawakoli T, Azarhoushang B (2017) Material removal mechanism in ultrasonic-assisted grinding of Al₂O₃ by single-grain scratch test. *Int J Adv Manuf Technol* 91:2949–2962. <https://doi.org/10.1007/s00170-016-9967-4>
28. Liang Z, Wang X, Wu Y et al (2013) Experimental study on brittle–ductile transition in elliptical ultrasonic assisted grinding (EUAG) of monocrystal sapphire using single diamond abrasive grain. *Int J Mach Tools Manuf* 71:41–51. <https://doi.org/10.1016/j.ijmachtools.2013.04.004>
29. Garcia Luna G, Axinte D, Novovic D (2020) Influence of grit geometry and fibre orientation on the abrasive material removal mechanisms of SiC/SiC Ceramic Matrix Composites (CMCs). *Int J Mach Tools Manuf* 157:103580. <https://doi.org/10.1016/j.ijmachtools.2020.103580>
30. Huang H, Li X, Mu D et al (2021) Science and art of ductile grinding of brittle solids. *Int J Mach Tools Manuf* 161:103675. <https://doi.org/10.1016/j.ijmachtools.2020.103675>
31. Qiao G, Yi S, Zheng W et al (2022) Material removal behavior and crack-inhibiting effect in ultrasonic vibration-assisted scratching of silicon nitride ceramics. *Ceram Int* 48:4341–4351. <https://doi.org/10.1016/j.ceramint.2021.10.229>
32. Khoran M, Azarhoushang B, Daneshi A (2021) Experimental study of single grit scratch test on carbon fiber-reinforced polyether ether ketone. *Prod Eng Res Devel* 15:751–759. <https://doi.org/10.1007/s11740-021-01056-0>
33. Zhang Z, Wang B, Kang R et al (2015) Changes in surface layer of silicon wafers from diamond scratching. *CIRP Ann* 64:349–352. <https://doi.org/10.1016/j.cirp.2015.04.005>
34. Patnaik Durgumahanti US, Vijayender Singh P, Rao V (2010) A new model for grinding force prediction and analysis. *Int J Mach Tools Manuf* 50:231–240
35. Singh V, Ghosh S, Rao PV (2011) Comparative study of specific plowing energy for mild steel and composite ceramics using single grit scratch tests. *Mater Manuf Processes* 26:272–281. <https://doi.org/10.1080/10426914.2010.526979>
36. Singh V, Paruchuri VR, Ghosh S (2012) Development of specific grinding energy model. *Int J Mach Tools Manuf* 60:1–13. <https://doi.org/10.1016/j.ijmachtools.2011.11.003>
37. Zahedi A, Azarhoushang B (2017) An analytical force and surface roughness model for cylindrical grinding of brittle materials. *IJAT* 8:68. <https://doi.org/10.1504/IJAT.2017.10007964>
38. Zhang Z, Wang X, Meng F et al (2022) Origin and evolution of a crack in silicon induced by a single grain grinding. *J Manuf Process* 75:617–626. <https://doi.org/10.1016/j.jmapro.2022.01.037>
39. CeramTec GmbH: advanced ceramics for mechanical engineering. www.ceramtec-group.com/en/press/press-downloads
40. Marinescu I (ed) (2006) Handbook of advanced ceramics machining. CRC Press
41. Tawakoli T, Azarhoushang B (2011) Intermittent grinding of ceramic matrix composites (CMCs) utilizing a developed segmented wheel. *Int J Mach Tools Manuf* 51:112–119. <https://doi.org/10.1016/j.ijmachtools.2010.11.002>
42. Paknejad M, Abdullah A, Azarhoushang B (2017) Effects of high power ultrasonic vibration on temperature distribution of workpiece in dry creep feed up grinding. *Ultrason Sonochem* 39:392–402. <https://doi.org/10.1016/j.ultsonch.2017.04.029>
43. Zhang Y, Zhu S, Zhao Y et al. (2022) A material point method based investigation on crack classification and transformation induced by grit geometry during scratching silicon carbide. *Int J Mach Tools Manuf*:103884. <https://doi.org/10.1016/j.ijmachtools.2022.103884>

Publisher's note Springer Nature remains neutral with regard to jurisdictional claims in published maps and institutional affiliations.